2018 EAGE ANNUAL
80TH CONFERENCE + EXHIBITION
COPENHAGEN | DENMARK

Tu E 16

Robust Estimation of CSEM Measurement Uncertainty at a Destructive Interference

J.P. Morten* (EMGS), M.A. Drage (EMGS), R. Mittet (EMGS)

Summary

Accurate estimation of CSEM measurement uncertainty is required for quantitative analysis in inversion, survey optimization, and feasibility studies. We describe a practical uncertainty model that robustly handles measured data even in a geology that gives rise to dramatic amplitude features. We explain how such features arise from interference effects, which clarifies CSEM shallow water wave propagation phenomenology.

Introduction

The marine controlled-source electromagnetics (CSEM) technology has diversified to include e.g. equipment sets with shallow-towed sources and towed receivers, and application in frontier and unusual geologies. Thus, we encounter remarkable data features not considered in standard literature, and which challenge common methods for data analysis. Robust quantification of measurement uncertainty is essential for feasibility studies and survey planning, where underestimation may lead to wrong conclusions regarding target sensitivity. Underestimation of the uncertainty can be a critical problem for inversion, leading to imaging artefacts or lack of convergence. The inversion objective function quantifies the data difference ratio to measurement error $\|\Delta E_i/\delta E_i\|_p$, and an unrealistically small δE_i will bias the model update to exaggerate outliers with high sensitivity to noise.

In this paper we present a practical model for CSEM measurement uncertainty estimation that robustly handles sudden amplitude variations. Our model can be motivated by the real-data example in Figure 1, which shows inline electric field amplitude data, $|E_x|$. The data was acquired in the Barents Sea using a shallow-towed, high-power source system (Barker et al., 2012). The formation resistivity is high, which makes it feasible to use high frequencies. The amplitude data exhibit a cusp at an offset that decreases with increasing frequency. The depression in amplitude is deeper for the higher frequencies. We will show later that this is caused by a destructive interference effect due to two different wave propagations. But first we focus on the prediction of the measurement uncertainty, δE_x. A simple estimate is achieved by a relative uncertainty proportional to the amplitude combined with an ambient noise contribution. The uncertainty prediction from such an estimate is shown as a thin line in Figure 1. At the cusp, this estimate significantly underestimates uncertainty. Small perturbations in source-receiver offset can give a large change in the data. The contribution to the inversion objective function at the cusp will be severely overestimated, and may dominate. We will describe an extension to the uncertainty model that explicitly incorporates a contribution from source-receiver offset uncertainty and overcomes this problem. The uncertainty estimate from this model is shown as the dashed line in Figure 1, and at 11.5 Hz we see that the uncertainty estimate at the cusp is increased by an order of magnitude, suppressing error-prone responses within a km-wide interval.

Uncertainty model

We will apply the error propagation framework described by Mittet and Morten (2012) to quantify the data uncertainty, δF_i. The quantity F_i can represent either an electric ($F = E$) or magnetic ($F = H$)

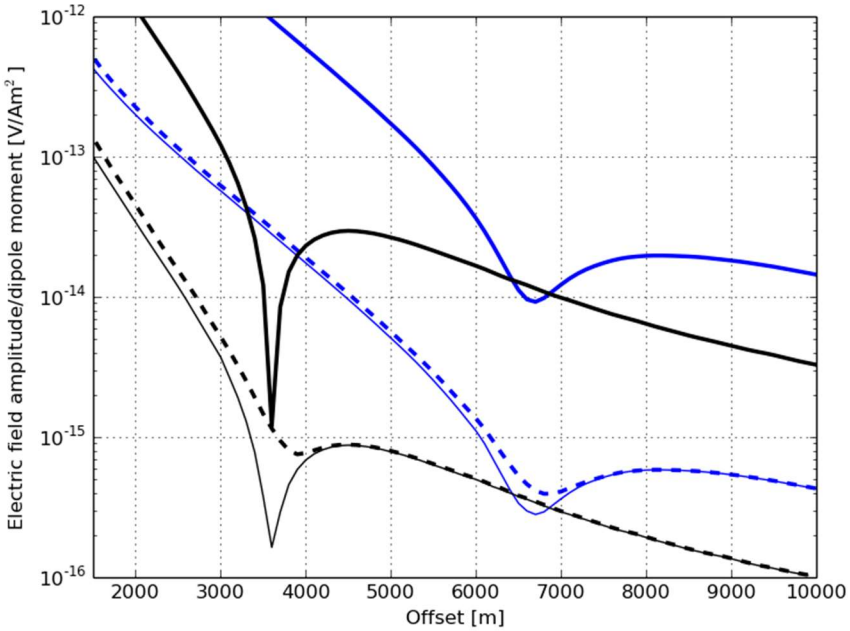

Figure 1 *Real-data example from the Barents Sea, Norway. Thick solid lines show inline electric field amplitude $|E_x|$: Blue – 3.5 Hz, black – 11.5 Hz. The dashed and thin lines show uncertainty estimates δE_x with and without contribution from a term determined by data derivative with offset.*

field component in direction $i = x, y$. As an approximation to the detailed model, Mittet and Morten (2012) investigated a simplified model incorporating a term that describes relative uncertainty with ratio γ, and an ambient noise term δN,

$$\delta F_i(\mathbf{r}) = \sqrt{\gamma^2 |F_i(\mathbf{r})|^2 + \delta N^2}\,. \tag{1}$$

We choose the origin at the receiver position and let $\mathbf{r}$ denote the source position. When extended with a term that describes receiver orientation uncertainty, $\delta\theta$, relevant for azimuth data (Morten et al., 2009), this is a practical uncertainty model that has provided a useful weight scheme for 3D CSEM inversion applied to data from surveys in different geologies. However, the model in Eq. (1) is not applicable for datasets where the amplitude $|F_i|$ variation drastically deviates from exponential like the example in Figure 1. The approximation fails to represent a term related to uncertainty in the source-receiver offset, δr, that is determined by the derivative of the data sample with respect to source-receiver offset $\partial F_i/\partial r$. The amended uncertainty model which includes the $\partial F_i/\partial r$ contribution from Mittet and Morten (2012) becomes

$$\delta F_i(\mathbf{r}) = \sqrt{\gamma^2 |F_i(\mathbf{r})|^2 + \delta N^2 + \left|\frac{\partial F_i(\mathbf{r})}{\partial \theta}\delta\theta\right|^2 + \left|\frac{\partial F_i(\mathbf{r})}{\partial r}\delta r\right|^2}\,. \tag{2}$$

The real parameter δr is determined by operational performance characteristics. For example, accurately positioning seafloor equipment is harder in deep water than in shallow water. The models in Eqs. (1) and (2) are shown as the thin and dashed lines respectively in Figure 1. Note that the term scaling with $\partial F_i/\partial\theta$ introduces a contribution proportional to the orthogonal field component (e.g. $|E_y|$ for δE_x), and for azimuth data this avoids the severe underestimation of uncertainty at the cusp feature. For inline data it is however essential to include the δr-contribution. The relative uncertainty γ in Eq. (2) represents the contributions due to e.g. sensor calibration and source output uncertainty, and can be predicted based on quantitative information about equipment performance.

To determine the uncertainty model contribution $|\partial F_i/\partial r|\delta r$ we need to compute the derivative of the field component F_i. For synthetic data this can be carried out very accurately by modeling the corresponding measurement at closely spaced source locations, and then constructing the finite-

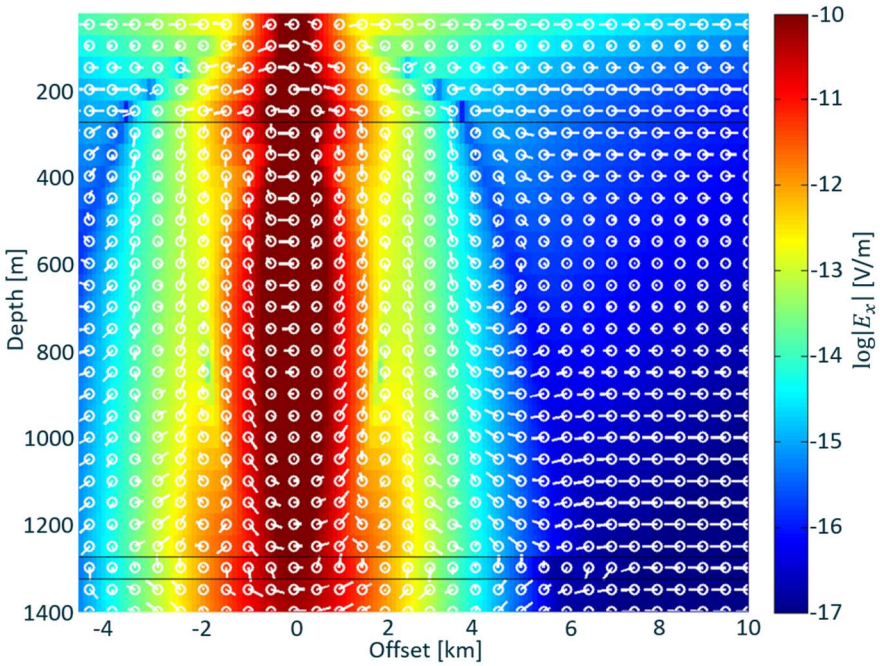

Figure 2 *Electric field in a plane-layer model at 17.8 Hz with the source at x=0 m, z=200 m. The color scale shows the horizontal electric field amplitude as* $\log|E_x|$. *The vector overlay (white lines with a circle at the vector origin) shows a snapshot of the harmonic time-variation* $\mathbf{E}(x,y=0,z;t)$ *at t=nT with period T=1/f. Black line at depth 250 m shows the location of the seafloor. The two black lines at depth 1250 m and 1310 m show the location of the resistive layer. Note the depression in* $|E_x|$ *at the seafloor about 3.5 km offset from the source, co-located with an electric field direction reversal. This corresponds to the cusp shown in the amplitude versus offset plot in Figure 3.*

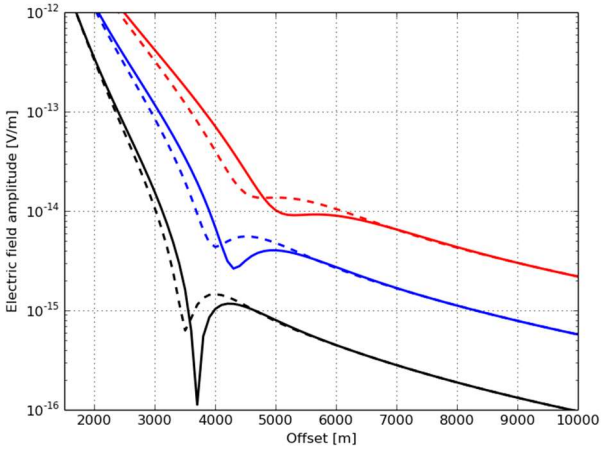

Figure 3 *Horizontal electric field amplitude for seafloor receivers in the model shown in Figure 2 (solid lines). The colors correspond to different frequencies: Red – 5.6 Hz, blue – 10 Hz, and black – 17.8 Hz. The dashed lines show the background field (no resistive target layer) for reference.*

difference derivative. For real data, such a procedure is constrained since the measurement locations are fixed by the survey layout. Moreover, the computation of a finite-difference derivative from real data will be affected by noise, which leads to the requirement that the variation between the data samples exceeds measurement uncertainty. We have found that the derivative can be estimated by considering consecutive source locations when data with dense spacing along the towline (~ 100 m) is available. In a general geometry with the towline offset from the receiver, the derivative can be approximated

$$\frac{\partial F_i(\mathbf{r})}{\partial r} \approx \frac{F_i(\mathbf{r}+\Delta\mathbf{l}) - F_i(\mathbf{r})}{\Delta l \cos(\alpha-\beta)}. \tag{3}$$

Here $\Delta\mathbf{l}$ is the displacement vector of the source for two consecutive source points, α is the line-of-sight angle from the receiver to the source, and β is the source heading. This estimate was used to compute the dashed uncertainty curve in Figure 1. Note that for broadside data where $\alpha - \beta = 90°$, the source displacement in radial direction $\Delta r \approx 0$ so the approximation breaks down, but in this case the uncertainty is dominated by other contributions and we can neglect $|\partial F_i/\partial r|\delta r$.

Interference effects in CSEM

To elaborate the physical phenomenology that gives rise to the measured cusp from Figure 1, we consider a plane-layer model synthetic data example. We consider inline electric field data, and set the water depth to 250 m. The receiver is on the seabed and the source towline is at 200 m depth. The water and uniform background resistivities are 0.31 Ωm and 8 Ωm respectively. These values are representative of the geology where the real-data example in Figure 1 was acquired. We also include a resistive layer at depth 1250 m that is 60 m thick and has resistivity 108 Ωm. We use the modelling approach described by Løseth and Ursin (2007) to compute the frequency-domain amplitude and phase of the electric field components, $|E_i(f)|e^{i\phi_i(f)}$, where f is the frequency. This determines the electric field from a harmonic source in a cross-section along the horizontal electric dipole source

$$\mathbf{E}(t) = |E_x(f)|\cos\big(\omega t - \phi_x(f)\big)\,\hat{\mathbf{x}} + |E_z(f)|\cos\big(\omega t - \phi_z(f)\big)\,\hat{\mathbf{z}}, \tag{4}$$

where we have suppressed the spatial arguments $(x, y = 0, z)$. The amplitude and direction of this field is shown in Figure 2. Note the region to each side of the source with a field direction reversal and an amplitude depression. At the seafloor, this feature is at 3.5 km source-receiver offset. Inside the resistive layer, the guided wave is dominant in $|E_z|$. This component is not shown in Figure 2, but the effect of the guided wave is clear in $|E_x|$ which is measured on the seafloor.

The $|E_x|$ field on seafloor receivers is shown in Figure 3. A feature similar to the cusp that was pointed out in the real data is apparent. To analyse this in detail we apply the decomposition into up- and down-going components described by Amundsen et al. (2006). We carry out the decomposition in the sea where the receivers are located. Note that for frequencies above 10 Hz, two-way propagation in the water column corresponds to more than 5 skin-depths. This gives two orders of magnitude reduction of field amplitude, making water column multiples a small contribution for high frequencies (Nordskag and Amundsen, 2010). The up-going component then represents subsurface response, and the down-going component is the airwave (Mittet and Morten, 2013). Figure 4 left shows that at the offsets where

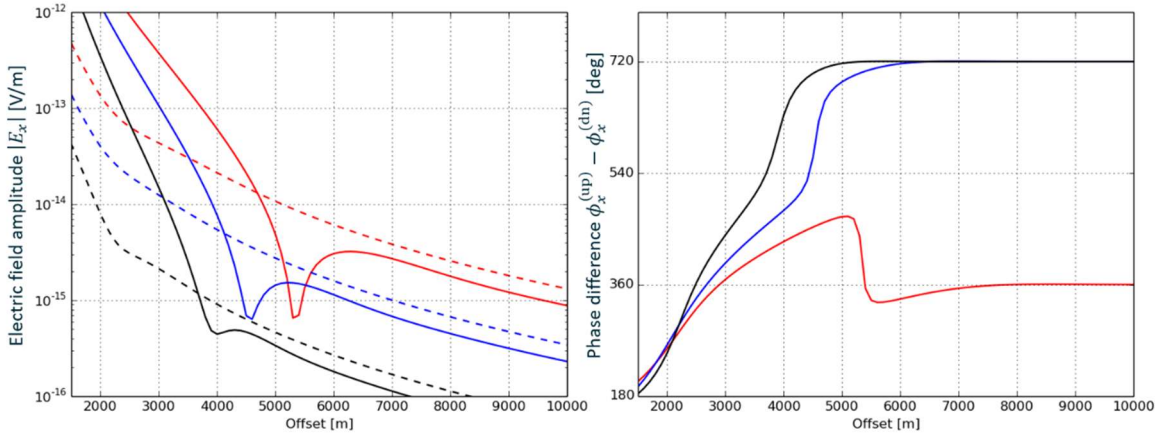

Figure 4 *Up-down separated electric field components for the target model data shown in Figure 3. Left: Amplitude with solid line up-going ($|E_x^{(up)}|$) and dashed line down-going ($|E_x^{(dn)}|$). Right: Phase difference between up-going and down-going components, $\phi_x^{(up)} - \phi_x^{(dn)}$.*

the cusp is observed (Figure 3), the up- and down-going components have similar amplitude. The E_x field follows from standard addition of harmonics,

$$A\cos(\omega t - \phi_A) + B\cos(\omega t - \phi_B) \overset{A\approx B}{\longrightarrow} 2A\cos\left(\frac{\phi_A - \phi_B}{2}\right)\cos\left(\omega t - \frac{\phi_A + \phi_B}{2}\right). \quad (5)$$

In this expression, $\phi_A - \phi_B$ corresponds to the phase difference shown in Figure 4 right. We see that at offset corresponding to the cusp in 10 Hz and 17.8 Hz data, the two contributions are out of phase, i.e. differ by a half-integer times 360° (540° in the plot). This leads to a classical destructive interference of the wave components according to Eq. (5) from the factor $\cos\left(\frac{\phi_A - \phi_B}{2}\right)$, which explains the cusp feature. A similar conclusion can be made without reference to up-down separation by explicitly modelling the primary contributions to the receiver signal. This further identifies the cusp in the 5.6 Hz $|E_x^{(up)}|$ data (Figure 4 left) as related to water column multiples.

Conclusions

We consider an uncertainty model for CSEM data that incorporates experimental errors scaling with a spatial derivative of the field. The contribution is important when destructive interference effects can cause simpler models to significantly underestimate measurement uncertainty. We demonstrate a practical implementation using real data. Finally, we explain the considered shallow-water wave propagation phenomenology using a synthetic data example. Our examples show that such interference effects occur in resistive environments for both shallow-towed and deep-towed source configurations.

Acknowledgements

We thank EMGS for permission to publish this paper.

References

Amundsen, L., L. O. Løseth, R. Mittet, S. Ellingsrud, and B. Ursin [2006] Decomposition of electromagnetic fields into upgoing and downgoing components, *Geophysics*, 71, no. 5, G211

Barker, N.D., J.P. Morten, and D.V. Shantsev [2012] Optimizing EM data acquisition for continental shelf exploration, *The Leading Edge*, 31(11), 1276

Løseth, L. O., and B. Ursin [2007] Electromagnetic fields in planarly layered anisotropic media, *Geophysical Journal International*, 170, 44

Mittet, R., and J. P. Morten [2012] Detection and imaging sensitivity of the marine CSEM method, *Geophysics*, 77, no. 6, E411

Nordskag, J.I. and L. Amundsen [2007] Asymptotic airwave modeling for marine controlled-source electromagnetic surveying, *Geophysics*, 72, no. 6, F249